

Biomimetic Molecule Catalysts to Promote the Conversion of Polysulfides for Advanced Lithium–Sulfur Batteries

Xinwei Ding, Shuo Yang, Suyu Zhou, Yingxin Zhan, Yuchong Lai, Xuemei Zhou, Xiangju Xu, Huagui Nie, Shaoming Huang, and Zhi Yang*

To overcome the shuttle effect in Li–S batteries, novel biomimetic molecule catalysts are synthesized by grafting hemin molecules to three functionalized carbon nanotube systems (CNTs–COOH, CNTs–OH, and CNTs–NH₂). The Li–S battery using the CNTs–COOH@hemin cathode exhibits the optimal initial specific capacity (1637.8 mAh g⁻¹) and cycle durability (up to 1800 cycles). Various in situ characterization techniques, such as Raman spectroscopy, Fourier-transform infrared reflection absorption spectroscopy, and UV–vis spectroscopy, combined with density functional theory computations are used to investigate the structure–reactivity correlation and the working mechanism in the Li–S system. It is demonstrated that the unique structure of the CNTs–COOH@hemin composite with good conductivity and adequate active sites resulting from molecule catalyst as well as the strong absorption to polysulfides entrapped by the coordinated Fe(III) complex with Fe–O bond enables the homogeneous dispersion of S, facilitates the catalysis and conversion of polysulfides, and improves the battery's performance.

the shuttle effect caused by the dissolution and migration of long-chain polysulfides (Li₂S_n, n = 4–8) generally leads to a rapid capacity decay and a low coulombic efficiency.^[7] Recently, major efforts have been made to introduce various mediator materials (e.g., metals,^[8] metal compounds,^[9] and emerging inorganic/organic complexes^[10,11]) into cathodes to address these issues, particularly the shuttle effect. Despite some successes, the improved performance that results from these heterogeneous mediators remains limited, especially at high areal sulfur loadings.^[1] Vast soluble Li polysulfides (LiPSs) rapidly form and accumulate on the surfaces of these heterogeneous mediators,^[12] coupling with the sluggish kinetics of the liquid–solid phase transformation from soluble LiPSs to solid Li₂S lead to poor electron and ion transport in the electrode

and electrolyte, resulting in a rapid capacity decay.^[13–15] Thus, the development of neoteric molecule mediators,^[12] which can rapidly eliminate or convert LiPSs, is highly desired to regenerate active sites containing S and to manage the shuttle effect of LiPSs.

Natural enzymes are exquisite biocatalysts that mediate every biological process in living organisms. They are able to accelerate the rate of chemical reactions by up to 10¹⁹ times for specific substrates and reactions.^[16] Inspired by the wisdom of nature, exploiting biocatalysts or their artificial analogues may be an ideal strategy to address the aforementioned issue. Hemin and its iron-porphyrin derivatives^[17] serve as the electroactive center of many heme-proteins and have been used in diverse applications involving oxygen transport^[18] and the detection of various species such as NO,^[19] NO₂⁻,^[20] and H₂O₂.^[21] Considering sulfur and oxygen belong to the same group of elements in the periodic table, we were motivated to investigate the result of introducing hemin or its modified derivative into a Li–S system.

Herein, we present a systematic design involving biomimetic molecule catalysts to promote the conversion of polysulfides for advanced Li–S batteries, in which hemin was grafted to carbon nanotubes (CNTs) modified with a functional group (FG) to form CNTs–FG@hemin composite. FG in this article indicates a NH₂, OH, or COOH group unless specified otherwise. When the CNTs–COOH@hemin composite was applied into the cathode as a biomimetic mediator, the battery delivered

1. Introduction

Lithium–sulfur (Li–S) batteries are regarded as next-generation energy storage systems because of their higher theoretical capacity, lower cost, and improved environmental benignity compared with those of traditional lithium-ion batteries.^[1–3] However, the practical application of Li–S batteries is obstructed by the poor electrical conductivity of sulfur and its insoluble discharge products (Li₂S or Li₂S₂) as well as the large volume fluctuation between S₈ and Li₂S.^[4–6] In particular,

X. Ding, Dr. S. Yang, S. Zhou, Y. Zhan, Y. Lai, Dr. X. Zhou, Dr. X. Xu, Prof. H. Nie, Prof. Z. Yang
Key Laboratory of Carbon Materials of Zhejiang Province
Wenzhou University
Wenzhou 325035, China
E-mail: yangzhi@wzu.edu.cn

Dr. S. Yang
College of Electrical and Electronic Engineering
Wenzhou University
Wenzhou 325035, China

Prof. S. Huang
School of Materials and Energy
Guangdong University of Technology
Guangzhou 510006, China

 The ORCID identification number(s) for the author(s) of this article can be found under <https://doi.org/10.1002/adfm.202003354>.

DOI: 10.1002/adfm.202003354

a high initial specific capacity of 1637.8 mAh g⁻¹ at 0.2 C with an ultralow-capacity degradation rate of 0.042% per cycle after 1800 cycles. In addition, the structures of the three composites and their working mechanisms in Li-S batteries, especially for CNTs-COOH@hemin composite, were systematically investigated using in situ vibrational spectroscopy, X-ray photoelectron spectroscopy (XPS), in situ UV-vis spectroscopy, and density functional theory (DFT) calculations, etc.

2. Results and Discussion

2.1. Structural Analysis of CNTs-FG@Hemin Composites

In this study, hemin was introduced into the Li-S cathode as a biomimetic mediator because of its high catalytic activity and good catalytic selectivity. In order to avoid hemin molecules from forming inactive aggregates and self-destructing during the oxidizing process and to improve the conductivity and catalytic activity of hemin,^[22,23] hemin molecules were grafted to CNTs modified with three different functional groups, i.e., CNTs-NH₂, CNTs-OH, and CNTs-COOH, using ultrasonication.^[24] Three self-assembled composites, CNTs-NH₂@hemin, CNTs-OH@hemin, and CNTs-COOH@hemin, were obtained, respectively, as schematically illustrated in Figure 1.

Because zeta potential is a function of the surface coverage of charged species in a given environment and is theoretically

determined by the number of charges on surface species,^[25] the charge distributions of the cathode materials in our study were briefly quantified using the zeta potential. First, we performed zeta potential tests for hemin, CNTs-FG, and CNTs-FG@hemin suspensions in dimethyl sulfoxide (DMSO). As shown in Figure S1 in the Supporting Information, the zeta potentials of CNTs-NH₂, CNTs-OH, and CNTs-COOH were 0.124, -0.107, and -0.889 mV, respectively. After introducing hemin molecules into the systems, the zeta potentials of CNTs-FG@hemin composite changed in different degrees and were shown to be -0.133, -0.052, and -0.107 mV for CNTs-NH₂@hemin, CNTs-OH@hemin and CNTs-COOH@hemin, respectively. It is important to note that the zeta potential of the CNTs-COOH@hemin changed significantly compared with those of the other two composites, i.e., CNTs-NH₂@hemin and CNTs-OH@hemin, which nearly approaches to the zeta potential of hemin, implying that hemin is more uniformly dispersed on CNTs-COOH and that it is tightly bound to the CNTs-COOH. The good dispersion in CNTs-COOH@hemin composite can provide a large number of active sites for anchoring and rapid conversion of polysulfides in the electrochemical reactions of Li-S battery.

To further analyze the detailed chemical structures of the CNTs-FG@hemin composites, a series of XPS measurements were performed. The survey spectra revealed the various elements presented on the surface: C, Fe, N, O, and Cl (as shown in Figure 2a-d and Figure S2 in the Supporting Information). For

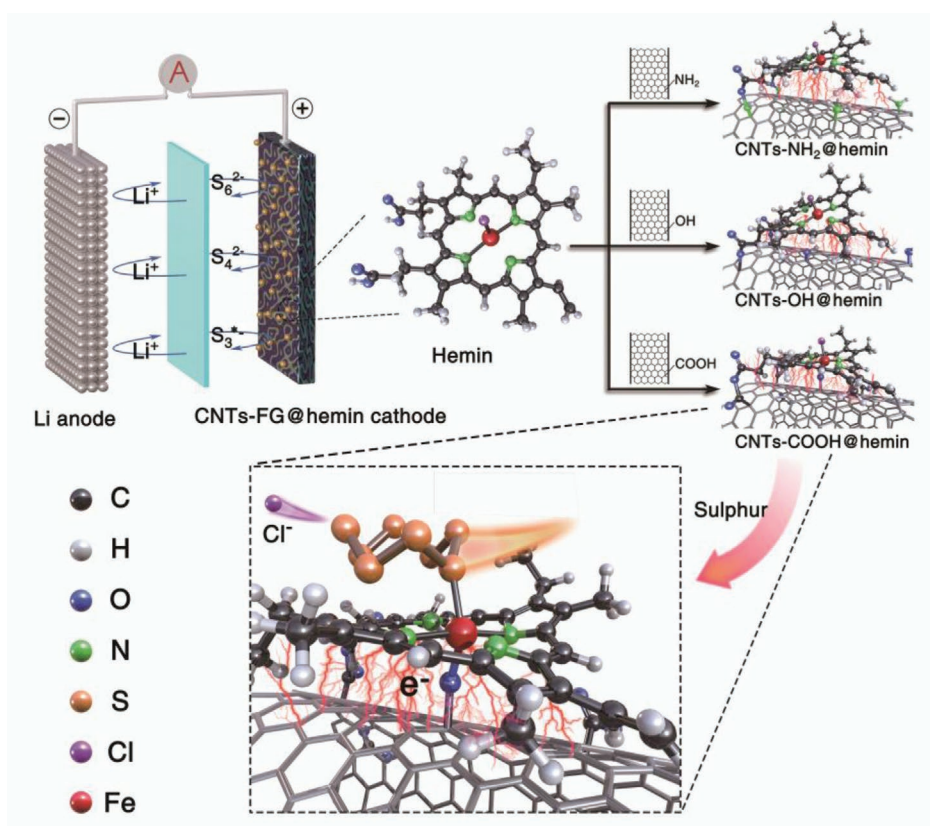


Figure 1. Schematic configuration of a Li-S battery based on three CNTs-FG@hemin cathodes (FG=NH₂, OH, COOH), and the mechanism of polysulfide adsorption at the CNTs-COOH@hemin cathode.

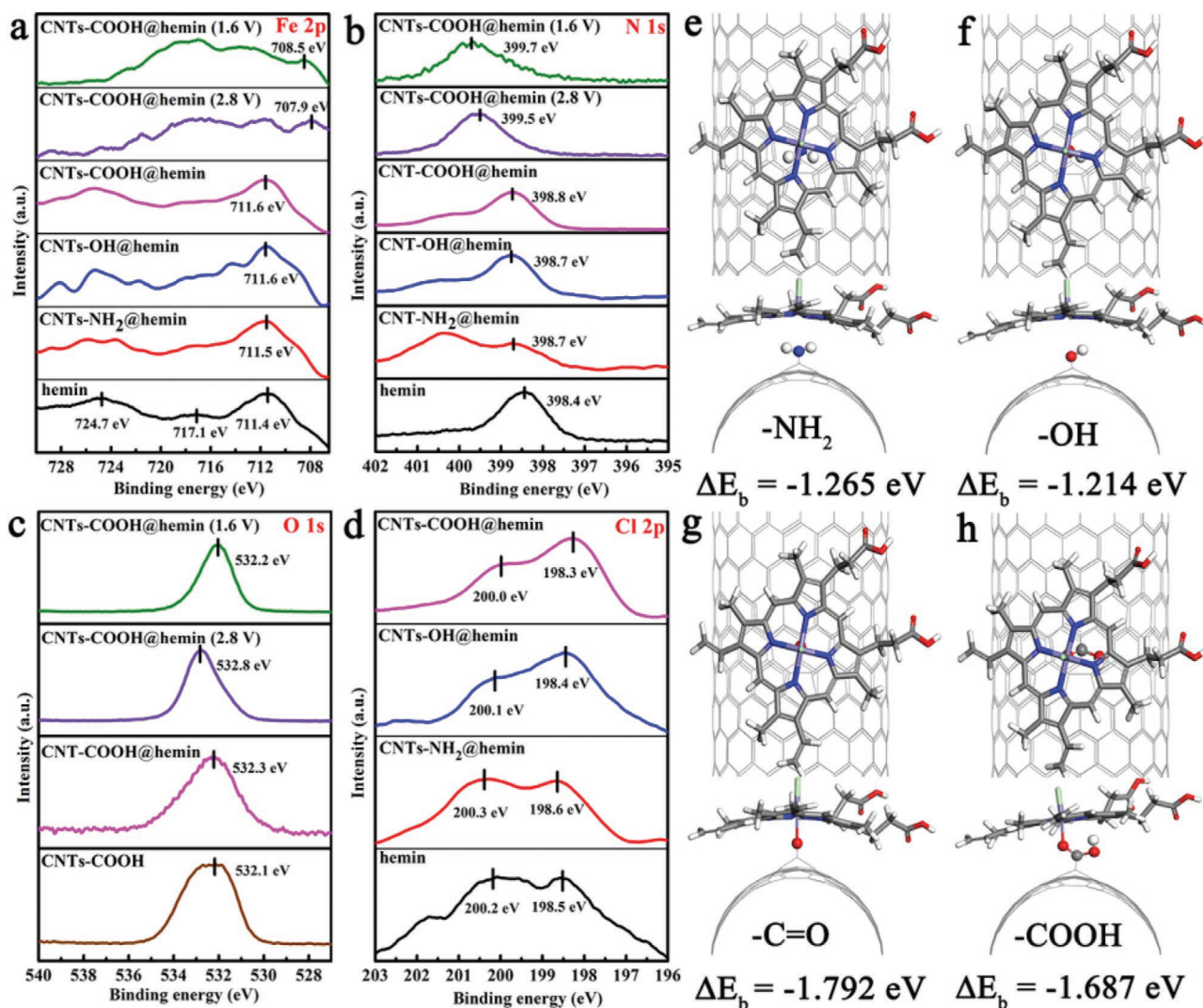


Figure 2. Chemical structure study of the composites: a) Fe 2p, b) N 1s, c) O 1s, d) Cl 2p XPS spectra of hemin and the composites. The structure and binding energy of e) CNTs-NH₂@hemin, f) CNTs-OH@hemin, g) CNTs-C=O@hemin, h) CNTs-COOH@hemin composites deduced from DFT analysis (For each system, the top figure is the top view and the bottom figure is the side view). The white, gray, red, blue, purple, wathet, and cyan sticks/balls are H, C, O, N, Li, Fe, and Cl atoms, respectively.

a hemin molecule, the C 1s spectrum (black curve in Figure S2, Supporting Information) showed a signal at 289.1 eV, which is attributed to the -COOH group of hemin. However, this peak was not observed in the spectra after hemin was grafted onto the CNTs-FG, as demonstrated by the red, blue, and pink curves in Figure S2 in the Supporting Information, most likely because of the formation of a coordinate bond between the -COOH group of hemin and the FG on the CNTs.^[22] The high-resolution Fe 2p XPS spectrum of hemin (black curve in Figure 2a) contained three peaks at 724.7, 717.1, and 711.4 eV, corresponding to Fe 2p_{1/2}, satellite, and Fe 2p_{3/2}, respectively. In contrast, the Fe 2p peaks in the CNTs-FG@hemin system shifted to higher field (the red, blue, and pink curves in Figure 2a). Similarly, compared with the N 1s XPS peaks of hemin (black curve in Figure 2b), the peaks shifted to higher field (red, blue, and pink curves in Figure 2b) when hemin was modified on the CNTs-FG. The XPS results indicate that π - π

conjugation has been formed between hemin and CNTs, causing the electrons to transfer from Fe and N to the CNTs. Moreover, the noncovalent interaction between hemin and the CNTs was also supported by DFT calculations. The charge transfer between the CNTs and hemin at the optimal configurations was simulated by Mulliken charge analyses.^[26] A weak charge (0.29 e) was observed to be transferred from the hemin monomer to the CNTs for the hemin/CNT system, suggesting the involvement of noncovalent interactions in the physisorption of the hemin molecules onto the pristine CNTs. Consequently, we summarized that two interactions existed in the CNTs-FG@hemin composite: coordinate bonding between hemin and the FG on the CNTs and π - π conjugation between hemin and CNTs, as illustrated in Figure 1.

Further analysis of the O 1s spectra of the CNTs-COOH and CNTs-COOH@hemin (brown and pink curves in Figure 2c) revealed that the C=O band (532.1 eV) of the CNTs-COOH

shifted to higher field by 0.2 eV, whereas the Cl 2p XPS spectra of the hemin and CNTs–COOH@hemin (black and pink curves in Figure 2d) revealed that the Cl 2p_{3/2} peak at 198.5 eV and Cl 2p_{1/2} peak at 200.2 eV shifted to lower field after hemin was grafted to the CNTs–COOH. These findings indicate that O from the –COOH functional group provides electrons for Cl from hemin through the new chemical bond between the centered Fe atom of hemin and the –COOH on the CNTs, thus resulting in weakening of the Fe–Cl bond. The DFT results in Figure 2g,h, Figure S3 and Table S1 in the Supporting Information directly revealed that an attractive bond was newly formed between the Fe atom centered in hemin and the O atom in the –COOH group or >C=O group (another possible form of the –COOH group in solution with higher energetic stability), and the bond length of Fe–O in the two binding complexes was approximately 2.019 Å. In other words, CNTs–COOH@hemin is a six-coordinated Fe(III) complex, where hemin is chemisorbed on CNTs–COOH via a newly formed Fe–O bond, as illustrated in Figure 1. The chemisorption of hemin also affects the lengths of the Fe–Cl and C–N bonds within the porphyrin ring, as shown in Table S1 in the Supporting Information. The DFT calculations corresponded well to the XPS results for O and Cl. In contrast, for the CNTs–NH₂@hemin and CNTs–OH@hemin systems, the Cl 2p XPS peaks (red and blue curves in Figure 2d) showed an opposite and smaller shift, respectively, which is responded by the results of their zeta potentials (Figure S1, Supporting Information). In addition, no new chemical bonds or special structural distortion were observed in the DFT results, as shown in Figure 2e,f and Figure S3 in the Supporting Information, suggesting that there is a weak physical interaction between hemin and the –NH₂/–OH groups on CNTs.

2.2. Electrochemical Performances of Li–S Batteries

To obtain insight into the electrochemical performance of Li–S batteries using four cathodes with or without hemin as mediator (named CNTs–NH₂@hemin cathode, CNTs–OH@hemin cathode, and CNTs–COOH@hemin cathode, and CNTs–COOH cathode, see Experimental Section), their cyclic voltammograms (CVs) were recorded using a scan rate of 0.1 mV s^{−1} in the potential range of 1.6–2.8 V, as shown in Figure 3a and Figure S4 in the Supporting Information. In these Figures, two pairs of distinct redox peaks were observed and became stable after the first cycle. The cathodic peaks at ≈2.3 V (P₁) and the anodic peaks at ≈2.4 V (P₄) are assigned to the transition between S and high-order polysulfides (Li₂S_n, n = 4–8), and the cathodic peaks at ≈2.05 V (P₂) and anodic peaks at ≈2.35 V (P₃) correspond to the transformation between Li₂S₄ and solid Li₂S/Li₂S₂.^[8,27,28] The large differences in the reduction and oxidation peaks between the first and second cycles are attributed to the rearrangement of the active sulfur from its original position to more energetically stable sites.^[29] Compared with the CVs of CNTs–COOH, CNTs–NH₂@hemin, and CNTs–OH@hemin cathodes (Figure S4, Supporting Information), the CV plots for the CNTs–COOH@hemin cathode in the subsequent two cycles were almost identical, as observed in Figure 3a, indicating that the CNTs–COOH@hemin cathode exhibits good electrochemical reversibility. A comparison of the CV curves of the

above four samples for the second cycle is shown in Figure 3b. From the inset of Figure 3b, it can be observed that the initial potential of the CNTs–COOH@hemin cathode was significantly more positive than those of the other three samples. Furthermore, the voltage hysteresis (ΔV, the value is obtained by subtracting the voltage at P₂ from the voltage at P₃) and collection coefficient (I_L/I_H, the peak current at ≈2.05 V (I_L) is associated with the formation of Li₂S, and the other peak current at ≈2.35 V (I_H) is associated with the formation of polysulfides) derived from the CV profiles in Figure 3b are summarized in Table S2 in the Supporting Information. The CNTs–COOH@hemin cathode had the lowest voltage hysteresis (ΔV), and its collection coefficient was the highest among those of the four samples. These results clearly demonstrate that the CNTs–COOH@hemin based Li–S cathode exhibits low polarizing voltage, high sulfur utilization, and effective suppression of the polysulfide shuttle effect.

The galvanostatic charge/discharge profiles of the four samples at a current rate of 0.2 C in Figure 3c consist of two well-defined discharge plateaus, which is consistent with the multistep electrochemical reaction of sulfur in the corresponding CV curves.^[30,31] The discharge plateaus of CNTs–COOH@hemin cathode were longer and flatter with a higher capacity than those of the other samples. Interestingly, the value of C₁ above 400 mAh g^{−1} approached the theoretical capacity of 418 mAh g^{−1} on the discharge platform, indicating that the CNTs–COOH@hemin composite can promote the conversion of LiPSs. In addition, higher reductions in the voltage plateaus and voltage hysteresis (ΔE, voltage gap between oxidation and reduction plateaus) were also observed for the CNTs–COOH@hemin cathode, which is consistent with the ΔV values of the CV plots.

A series of experiments were performed to evaluate the effect of the mass ratio of hemin (Figure S5, Supporting Information). The results indicate that the battery performance is optimal when hemin accounts for 1 wt% of the cathode mass. Figure 3d shows the rate capacities of the four cathodes for currents ranging from 0.2 to 3 C. Compared with the other three cathodes, the CNTs–COOH@hemin cathode exhibited much higher discharge capacity of 16378 mAh g^{−1} at 0.2 C, which approaches the theoretical capacity of 1675 mAh g^{−1}, and is better than most previous reports (Table S3, Supporting Information). Upon increasing the current, the capacities slowly decreased to 1058.0, 968.4, 910.7, and 873.4 mAh g^{−1} at 0.5, 1, 2, and 3 C, respectively. Because cycling stability is an important factor in assessing the performance of Li–S batteries, the prolonged cycling results from the CNTs–COOH and CNTs–FG@hemin cathodes at a current of 1 C are shown in Figure 3e. After 1800 charge/discharge cycles, the CNTs–COOH@hemin cathode still had a specific capacity of 205 mAh g^{−1}, and the corresponding average decay rate per cycle was as low as 0.042%. Such long cycles and low capacity retention have rarely been reported in Li–S battery field (Table S3, Supporting Information). The specific capacity after 1800 charge/discharge cycles remains higher than that of the traditional LiCoO₂ battery.^[32] Additionally, high sulfur loading is critical for achieving a high area capacity and volumetric energy density. As shown in Figure 3f, the CNTs–COOH@hemin cathode with a sulfur areal loading of 6.52 mg cm^{−2} exhibited a high areal capacity of 6.63 mAh cm^{−2} at a current density of 0.55 mA cm^{−2} and

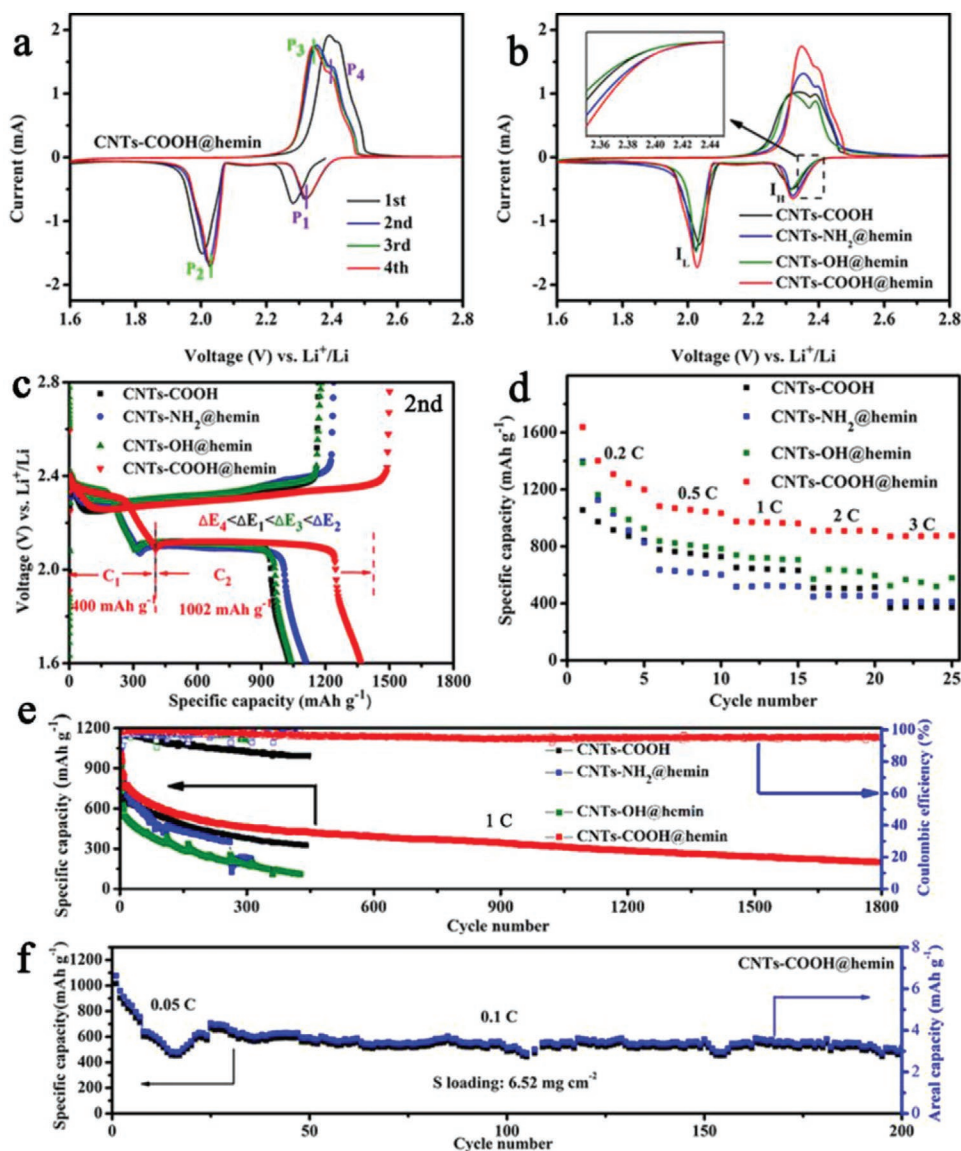


Figure 3. Electrochemical characterizations of CNTs-FG@hemin and CNTs-COOH cathodes in Li-S batteries: a) The first four cycles of CV profiles for CNTs-COOH@hemin cathode at a scan rate of 0.1 mV s^{-1} . b) The second cycle of CV profiles for CNTs-COOH, CNTs-NH₂@hemin, CNTs-OH@hemin, and CNTs-COOH@hemin cathodes recorded at a scan rate of 0.1 mV s^{-1} . Inset is higher magnification of the reduction current between 2.35 and 2.45 V. c) Galvanostatic charge-discharge profiles of the CNTs-COOH, CNTs-NH₂@hemin, CNTs-OH@hemin, and CNTs-COOH@hemin cathodes from the second cycle at 0.2 C. d) The rate capacity of CNTs-COOH, CNTs-NH₂@hemin, CNTs-OH@hemin, and CNTs-COOH@hemin cathodes. e) Cycling stability and Coulombic efficiency of CNTs-COOH, CNTs-NH₂@hemin, CNTs-OH@hemin, and CNTs-COOH@hemin cathodes at 1 C. f) Long-term cycling performance of CNTs-COOH@hemin cathode with a sulfur mass loading of 6.52 mg cm^{-2} measured at a rate of 0.05 C for the first 10 cycles and 0.1 C for the subsequent cycles.

maintained a high areal capacity of 3.46 mAh cm^{-2} at a high current density of 1.09 mA cm^{-2} after 200 cycles, making CNTs-COOH@hemin promising for real-world applications for competitive electrochemical energy storage systems.

2.3. Microstructural Mechanisms of CNTs-FG@Hemin Electrode Interfaces in Li-S Batteries

In situ vibrational spectroscopies applicable to electrochemical interfaces have great advantages in inspiring a profound

understanding of the detailed structural behaviors of interfaces in electrochemical environments. To better explore the relationship between the catalytic activity and structures of cathode materials, in situ Raman spectroscopy^[33] and Fourier-transform infrared reflection absorption spectroscopy (FT-IRAS)^[34] were used to evaluate the electrode/electrolyte interface in the Li-S battery systems. After the third electrochemical cycle, a series of potential-dependent Raman and IR spectra for the CNTs-COOH@hemin electrode/electrolyte interfaces were obtained in a stepwise fashion as a function of the potential with a 0.1 V interval through the discharge and charge

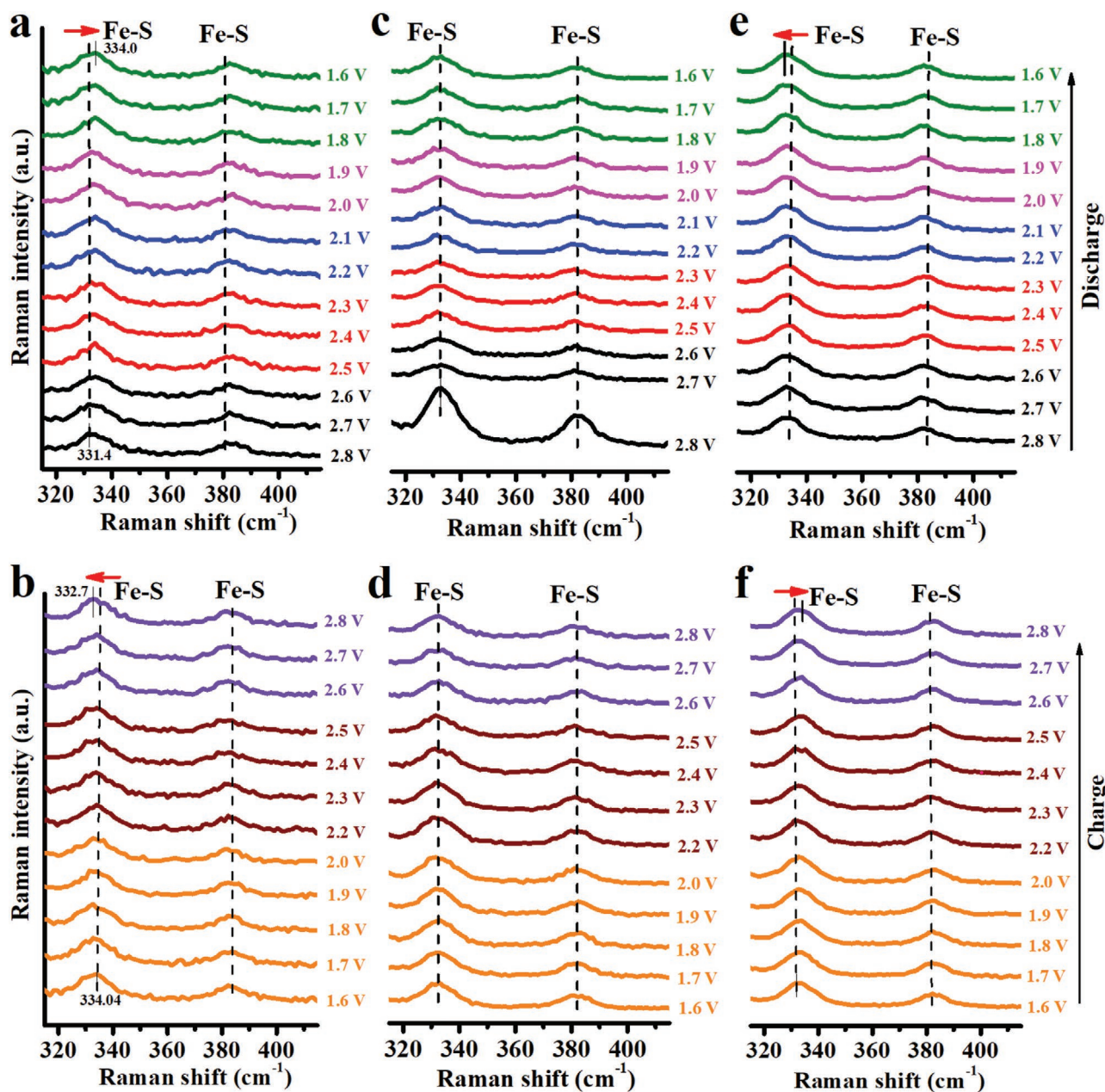


Figure 4. In situ Raman spectra of a) CNTs-COOH@hemin, c) CNTs-OH@hemin and e) CNTs-NH₂@hemin electrodes shown at respective potentials during discharge from 2.8 to 1.6 V and b,d,f) after recharging to 2.8 V, respectively.

processes, as shown in Figures 4a,b and 5a,c, where the spectra in potential region I ($2.5 \text{ V} < E < 2.8 \text{ V}$), II ($2.2 \text{ V} < E < 2.5 \text{ V}$), III ($2.1 \text{ V} < E < 2.2 \text{ V}$), IV ($1.8 \text{ V} < E < 2.1 \text{ V}$), V ($1.6 \text{ V} < E < 1.8 \text{ V}$), VI ($1.6 \text{ V} < E < 2.1 \text{ V}$), VII ($2.1 \text{ V} < E < 2.6 \text{ V}$), and VIII ($2.6 \text{ V} < E < 2.8 \text{ V}$) are shown in black, red, blue, pink, green, orange, brown, and purple, respectively, to facilitate comparison with the CV curves in Figure 5b,d.

To verify whether the Fe atom centered in hemin interacts with the LiPSs, Raman spectra in the Fe-S stretching region for CNTs-COOH@hemin electrode were obtained. The presence of the peaks at ≈ 330 and 385 cm^{-1} in the Raman spectra of Figure 4a,b, which are attributed to Fe-S bonding vibrations

according to previous Raman studies,^[35,36] supports the hypothesis that the weak Fe-Cl bond in hemin is cleaved and that each Cl atom is replaced by an S atom, causing the formation of Fe-S coordinated bonds while LiPSs interact with the CNTs-COOH@hemin. This finding was also confirmed by the Cl 2p XPS results as shown in Figure S6 in the Supporting Information, where the Cl 2p peaks disappeared as Cl was replaced by LiPSs after several cycles. It is worth noting that the Fe-S Raman peaks in Figure 4a slightly shifted toward higher wavenumber as the potential scanned negatively, whereas the peaks returned to lower wavenumber as the potential was moved in the positive direction (Figure 4b), reflecting the

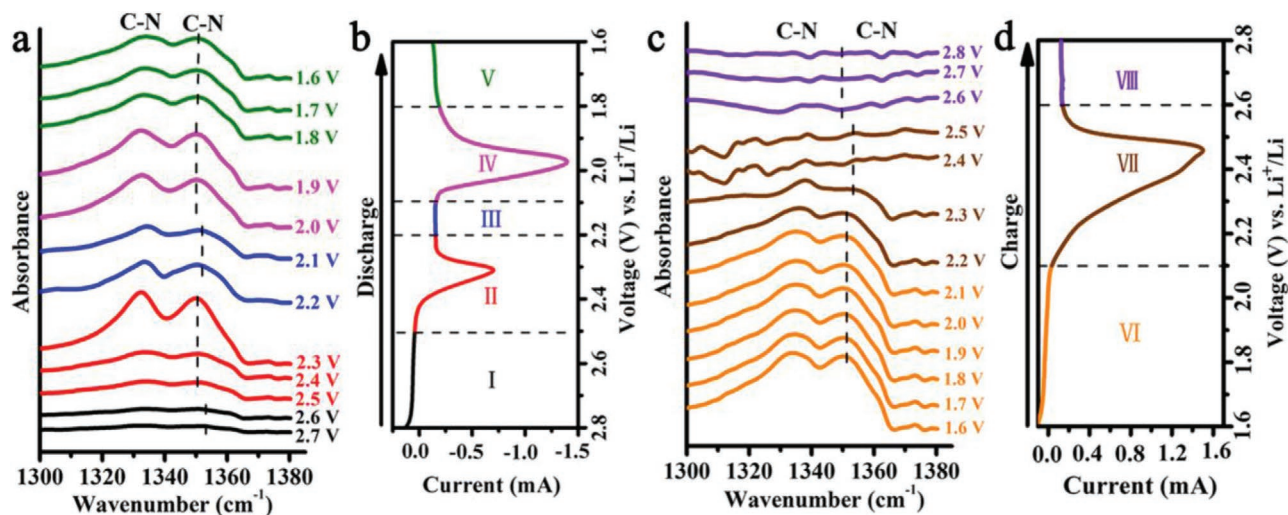


Figure 5. a) In situ IR spectra of CNTs-COOH@hemin electrodes shown at respective potentials during discharge from 2.8 to 1.6 V and c) after recharging to 2.8 V. The CV profiles corresponding to the b) discharge process and d) charge process.

strong electron transfer between Fe and LiPSs. Examination of the Raman spectra of the CNTs-OH@hemin (Figure 4c,d) and CNTs-NH₂@hemin electrodes (Figure 4e,f) revealed no peak shift and an opposite peak shift compared with that of CNTs-COOH@hemin electrode, apparently suggesting that no or only weak electronic interactions between Fe and LiPSs occur in CNTs-OH@hemin and CNTs-NH₂@hemin systems, respectively, more likely because of the lack of the coordinated Fe-O bond formation between the Fe atom of hemin and the FG on the CNTs as well as the effect of their different zeta potentials. Additional evidence of the electron transfer between Fe and LiPSs can be observed in the Fe 2p XPS spectra of the CNTs-COOH@hemin electrode obtained in fully discharged (1.6 V) and charged (2.8 V) states, as indicated by the green and purple curves in Figure 2a. When the electrode potential was maintained at 2.8 V (purple curve in Figure 2a), both the Fe 2p_{1/2} and Fe 2p_{3/2} peaks showed a significant shift towards lower energy compared with the XPS peaks obtained from CNTs-COOH@hemin composites (pink curve in Figure 2a). The shifting of the Fe 2p XPS peaks can most likely be attributed to the coordination between Fe and LiPSs,^[29,36] where the S atom provides an electron to the Fe atom and makes the Fe is in an electron-rich state. After finishing discharging at 1.6 V (green curve in Figure 2a), the peaks exhibited a small back shift towards higher energy because of the electron transfer from Fe to S caused by the conversion from the S substance to LiPSs.

In situ FT-IRAS was further employed to monitor the effect of Fe-S coordination on the structure of the CNTs-COOH@hemin electrode during discharge and charge. Figure 5a presents the potential-dependent IR spectra for CNTs-COOH@hemin electrode during discharge. The reference potential was set at 2.8 V, where no reaction occurred (Figure 3a). Upon changing the sampling potential in the negative direction, one pair of upward characteristic bands of adsorbed hemin appeared at ≈1330 and 1350 cm⁻¹ in the IR spectra, corresponding to the stretching vibrations of C-N bonds in hemin.^[37,38] The band intensity of the two bands started to increase at ≈2.5 to 2.3 V

(potential region II); in addition, the positions of the bands slightly shifted to lower wavenumber in this potential range. As the potential became more negative (potential region III), the intensity decreased rapidly up to 2.1 V, accompanied by a shift back of the band position. Then, the intensity increased and the band wavenumber gradually became lower as the potential changed from 2.1 to 1.9 V (potential region IV). When the potential was more negative than 1.9 V (potential region V), the intensity decreased and became constant, and the band position shifted to its original value. The increased intensities of the C-N band near 2.3 and 2.0 V, where S is transformed into short-chain LiPSs and further transformed into solid Li₂S/Li₂S₂, can be interpreted as an increase in the number of C-N dipoles in the normal direction at certain potentials according to the surface dipole selection rule.^[39] This finding suggests that the hemin molecule in our system does not exist in a planar porphyrin ring structure as usual but may be tilted slightly out of plane with an angle of θ due to the pulling of Fe-S bonding once a Cl atom is removed, as depicted in Figure S7 in the Supporting Information, where θ is the angle between the C-N axis and the surface direction. In such a structure, not only does the coordinating Fe provide electrons to LiPSs during discharge, as revealed by the XPS results (purple curve in Figure 2a), but N atoms in hemin also donate electrons to LiPSs through the Fe atom, as directly demonstrated by the shift of the N 1s XPS peak in the discharged state towards higher energy (green curve in Figure 2b) relative to the peaks for the fully charged (purple curve in Figure 2b) CNTs-COOH@hemin electrode and uncharged (pink curve in Figure 2b) CNTs-COOH@hemin composite. Therefore, it is reasonable to assume that there is a strong electronic interaction between Fe and LiPSs, resulting in a stronger Fe-S bond and a weaker adjacent C-N bond. That is why the position of the C-N band shifted to lower wavenumber, as observed in Figure 5a. Further evidence of this stronger Fe-S bond is also provided by the observed blue shift of the Fe-S bands with the negative-going potential scan in the Raman spectra (Figure 4a). Moreover, a redistribution of electrons in the CNTs-COOH@hemin

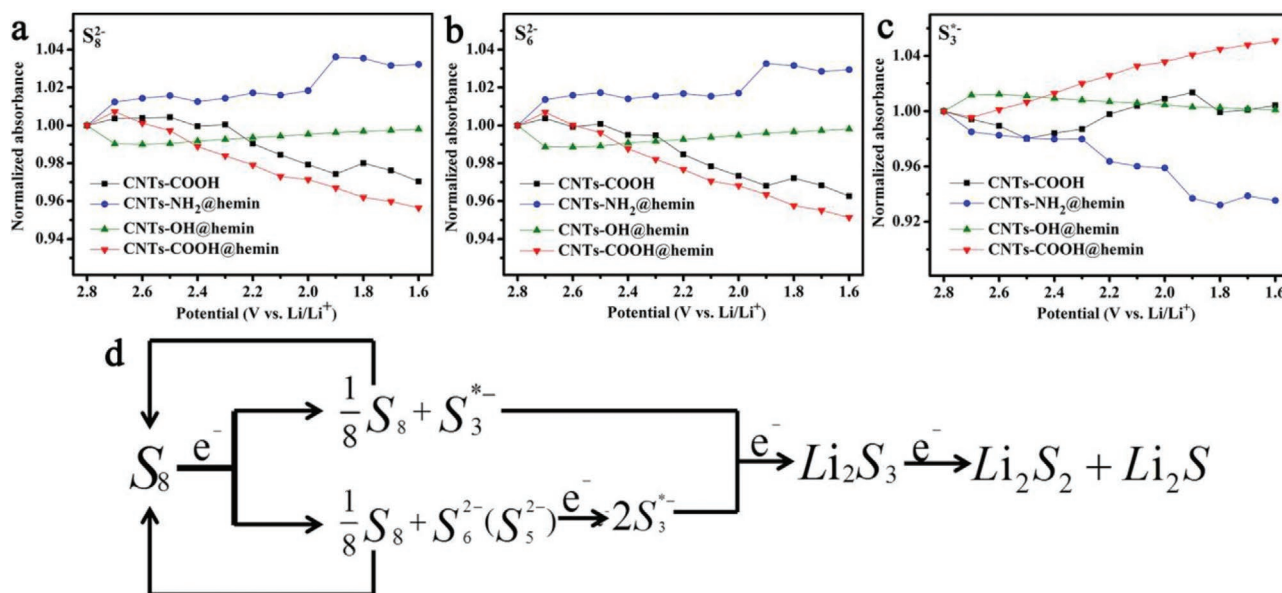


Figure 6. In situ UV-vis spectroscopic study of catalytic mechanism: The normalized absorbance of a) S_8^{2-} , b) S_6^{2-} , c) S_3^{*-} as a function of potential at different electrodes surfaces during discharge. d) The proposed sulfur reduction reaction pathways in our Li-S battery.

system due to the electron transfer effect may occur and increase the C–N dipole moment. Or, alternatively, in terms of molecular structure, the angle θ between the C–N axis and surface could increase under the pull of the stronger Fe–S bond, giving rise to the increased surface normal component of the C–N dipoles and thus resulting in increased intensity of the C–N bond in the IR spectra. The opposite trend is true for the charge process, as observed in Figure 5c, where the Fe–S band shifted to lower wavenumber and the C–N bands shifted to higher wavenumber and decreased in intensity as the potential changed in the positive direction.

Based on the results discussed above, the kinetics of the molecular structure at the CNTs–COOH@hemin surface during catalytic processes can be summarized as follows. When LiPSs in the electrolyte interact with the CNTs–COOH@hemin electrode during electrochemical reactions, the Fe atom centered in hemin gets rid of the Cl atom and acts as the binding site to anchor and catalyze polysulfide species, forming a Fe–S coordinated bond.^[40] In addition, the original planar porphyrin ring structure of hemin is broken and the C–N axis forms an angle of θ to the surface. During discharge and charge, electron transfer between Fe and LiPSs changes the bond strength of Fe–S and C–N and the surface normal components of the C–N dipoles due to the pulling of the Fe–S bond or an electron redistribution effect.^[36]

Apart from the surface molecular structures of CNTs–FG@hemin electrodes during catalysis, the evolution of polysulfides at different electrodes during discharge in Li_2S_8 solution was also monitored using in situ UV-vis spectroscopy.^[41] The UV-vis spectra are presented in Figure S8 in the Supporting Information, where the three primary bands at ≈ 475 , 492, and 617 nm are attributed to S_6^{2-} , S_8^{2-} , and S_3^{*-} species,^[40] respectively. The intensities of the absorbance for each measured UV-vis spectrum in Figure S8 in the Supporting Information at 492, 475, and 617 nm were collected and plotted as a function

of potential in Figure 6a–c. The intensities from different samples were normalized according to the absorbance of the first spectrum at 2.8 V. From Figure 6a–c, it can be observed that the CNTs–COOH@hemin electrode generally contained a lower concentration of long-chain polysulfides, i.e., S_8^{2-} and S_6^{2-} , but a higher concentration of short-chain polysulfides, i.e., S_3^{*-} , than those of the other electrodes. We attributed the appearance of more short-chain polysulfides to the faster catalytic conversion of long-chain polysulfides into short-chain polysulfides in the battery with the CNTs–COOH@hemin cathode.^[42]

Electrochemical impedance spectroscopy (EIS) experiments were further conducted to verify the above deduction. Nyquist curves and fitting curves in the uncycled state (fresh) and after 50 cycles (50th) and 150 cycles (150th) at a current of 1 C are presented in Figure S9a–h in the Supporting Information. The charge-transfer resistance (R_{ct}) is an important parameter in EIS analysis and can be determined from the semicircle in the high-frequency zone.^[43] As observed in Figure S9i,j and Table S4 in the Supporting Information, the CNTs–COOH@hemin cathode exhibited a lower R_{ct} in the fresh state than those of the other cathodes, and its R_{ct} value continued to decrease during 150 cycles, indicating that the addition of CNTs–COOH@hemin composite can improve the conductivity of the cathode, which is helpful for effectively regulating the interface, rapidly converting long-chain polysulfides, and optimizing the electron transport channel during the cycle.

With the help of DFT calculations of the CNTs–COOH@hemin electrode/electrolyte system, the reaction kinetics of the trapping and reduction of polysulfides by CNTs–COOH@hemin was further analyzed. At the very beginning of the discharge state (Figure 7a), the five-coordinated Fe(III) atom with Fe–O bond could accommodate the ring-like octatomic molecules (S_8), combined with the synergistic immobilization effect of chemical bonding and hydrogen bonding (Fe–S and $H \cdots S$), resulting in a high absorption rate and charge-transfer

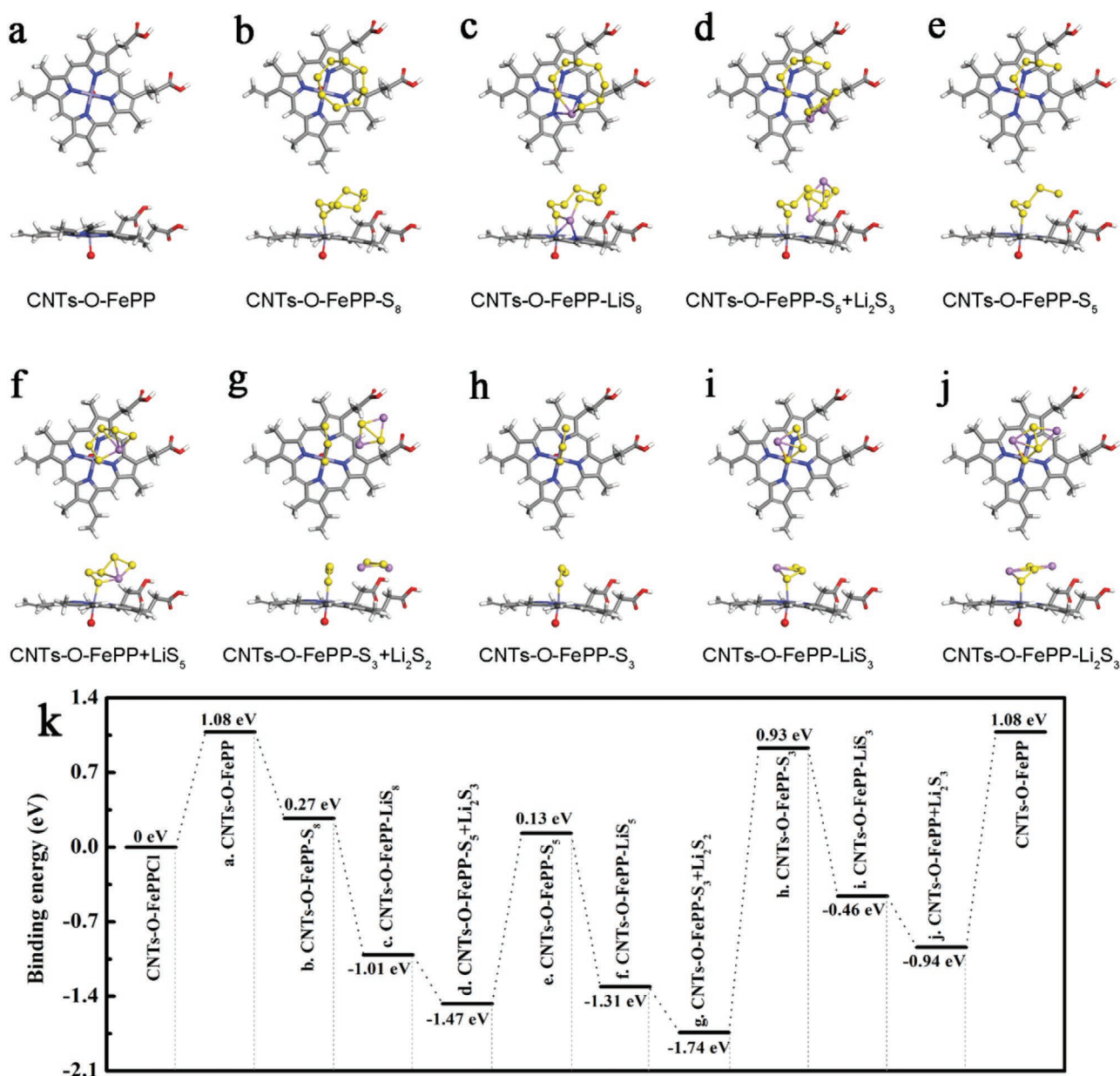


Figure 7. DFT calculations of the sulfur reduction kinetics on CNTs-COOH@hemin surface: a–j) Top and front views of the final optimized geometries of LIPs coordinated to Fe center of FePP/CNTs representing polysulfide reducing process. k) Energy diagram for the conversion of polysulfides on the CNTs-COOH@hemin.

efficiency. Figure 7b shows the binding structure of S₈ to the CNTs-O@hemin complex; ΔE_b was 0.27 eV (as shown in Figure 7k). As lithiation progressed, the ring structure of S₈ split into short-chain pieces, corresponding to the formation of strong chemical bonds of Li–S. Figure 7c shows the bonding of a Li ion to S₈, resulting in the cleavage of the octatomic ring in the molecular plane; its binding energy decreased to –1.01 eV (Figure 7k). Then, Li₂S₃ was formed (as shown in Figure 7d), and ΔE_b reached –1.47 eV (Figure 7k); in addition, the chain-like S₅^{2–} moiety was still fixed at the Fe center, and the other end was stabilized by H···S bonds, as illustrated in Figure 7e, after Li₂S₃ was removed from the ferriprotoporphyrin (FePP) molecular plane. As lithiation continued, the binding energies of

the S₅^{2–} fragment with Li ions became stronger compared with those of S₈. Because of the absence of the ring structure and reduction in the number of H···S hydrogen bonds (Figure 7f), S₅^{2–} soon split into S₃^{2–} and Li₂S₂ moieties (Figure 7g). After Li₂S₂ was diverted from the catalytic center, S₃^{2–} was the most stable and dominant intermediate in the system, as observed in Figure 7h; this finding agrees well with our in situ UV–vis experimental results (Figure 6c). Subsequently, S₃^{2–} underwent an electrochemical reduction to form LiS₃ and/or Li₂S₃, as observed in Figure 7i,j, or even Li₂S₂ and Li₂S. The overall reaction mechanism is illustrated in Figure 6d and is consistent with previous literature reports.^[43,44] Both our experimental and theoretical results suggest that the hemin on CNTs-COOH could

stabilize the LiPS species (Li_2S_n) in organic electrolytes by forming $\text{Fe}-\text{S}$, $\text{O}\cdots\text{Li}_2\text{S}_n$, and $\text{Li}_2\text{S}_n\cdots\text{H}$ bonds, and facilitates chemical equilibrium reactions to generate S_3^{2-} (or S_3^{*-}), therefore greatly suppressing the shuttle effect in Li-S batteries.

3. Conclusion

We successfully synthesized a high-performance biomimetic mediator for Li-S batteries by grafting the hemin bioenzyme onto CNTs-COOH. Various experimental characterization techniques, including zeta potential analysis, XPS, in situ Raman spectroscopy, FT-IRAS, and UV-vis spectroscopy, combined with detailed DFT computations were used to investigate the structure-reactivity correlation in Li-S batteries using CNTs-COOH@hemin composites. The findings indicate that this novel composite inherits the advantages of both CNTs-COOH and hemin. The CNTs-COOH improve the conductivity and dispersivity of sulfur by forming $\pi-\pi$ conjugation and coordinate bonds with hemin; in addition, the CNTs-COOH@hemin with a high adsorbing ability of polysulfides via the coordinated Fe(III) complex with Fe-O bond can promote faster conversion of long-chain polysulfides (S_8^{2-}) into abundant S_3^{2-} (or S_3^{*-}) during discharge, and can effectively suppress the shuttle effect in Li-S batteries. Using this new material, a high initial specific capacity of $1637.8 \text{ mAh g}^{-1}$ at 0.2 C, good long-term cycling performance, and fading rates as low as 0.042% per cycle up to 1800 cycles were achieved, which are superior to those of the other additives, CNTs-NH₂@hemin and CNTs-OH@hemin composites. We believe that the novel composite may open a pathway for the design of related materials using bioenzymes, which will have great potential applications for energy storage and catalysis.

4. Experimental Section

Synthesis of CNTs-FG@Hemin Cathode: The CNTs-FG-S composites were fabricated using a typical melt-diffusion approach. Briefly, the mixture of CNTs-FG (inside diameter: 3–5 nm, FG=NH₂, OH, COOH, functionalization degree = 1.14 wt% (CNTs-NH₂), 1.35 wt% (CNTs-OH), 1.23 wt% (CNTs-COOH), length = 10–20 μm , G/D ratio = 1.34 (CNTs-NH₂), 1.28 (CNTs-OH), 1.22 (CNTs-COOH), XFNano) and sulfur powder (>99.99%, metal basis, Aladdin) with a mass ratio of 7:3 was milled and placed in a sealed flask at 155 °C for 24 h to obtain the CNTs-FG-S hybrids. The CNTs-FG-S (80 wt%), CNTs-FG@hemin (15 wt%) and polyvinylidene difluoride (PVDF, 5 wt%) were then mixed in NMP and stirred for 8 h. Finally, the three CNTs-FG@hemin based sulfur cathodes (defined as the CNTs-FG@hemin cathodes in this paper) were obtained by pasting the slurry onto aluminum foil and drying at 55 °C overnight. The sulfur content of CNTs-COOH-S composites was determined to be 67.7 wt% by thermogravimetric analysis (TGA) measurements (Figure S10, Supporting Information). Therefore, the sulfur content in CNTs-COOH@hemin cathodes could be calculated as 54.2 wt% (80 wt% \times 67.7 wt%). To evaluate the effect of the content of hemin on the electrochemical performance of the electrode, a series of CNTs-COOH@hemin composites were prepared by changing the mass ratio of hemin to CNTs-FG (hemin: CNTs-FG = 0.5 wt%:14.5 wt%, 1 wt%:14 wt%, 2 wt%:13 wt%, 5 wt%:10 wt%).

Zeta Potential Tests of Hemin, CNTs-FG, and CNTs-FG@Hemin: Zeta potential measurements were performed on a ZetaSizer Nano ZS90 (Malvern Analytical). The suspensions used for the zeta potential

measurements were prepared by ultrasonically dispersing 2 mg of CNTs-FG or CNTs-FG@hemin in 10 mL of dimethyl sulfoxide (DMSO, 99.9%, Aladdin).

Electrochemical Measurements: Electrochemical performance studies were performed using CR2025 coin cells assembled in an argon-filled glove box. The CR-2025 coin cells consisted of the CNTs-FG@hemin cathodes, a porous membrane (Celgard 2400) as the separator, Li foil as the anode, and a 1 M solution of lithium bis(trifluoromethanesulfonyl) imide (LiTFSI) with 1 wt% LiNO₃ in 1,3-dioxolane (DOL) and 1,2-dimethoxy ethane (DME) (1:1, v/v) as the electrolyte. Both areas of cathode and anode are 1.53 cm², and the electrolyte/sulfur ratio is about 20:1 (mL mg⁻¹). Considering the experimental reproducibility, ten cells were prepared and tested at the same working conditions. The discharge/charge measurements were conducted in the voltage range of 1.6–2.8 V using a Neware battery test system (Shen Zhen Neware Technology). CV and EIS measurements were performed on a CHI760E electrochemical workstation (Chenhua (CH) Instruments).

In Situ Raman Spectroscopy Measurements: In situ Raman spectroscopy measurements were performed using a Renishaw inVia Raman microscope system (Renishaw, UK). A semiconductor laser operating at $\lambda = 532 \text{ nm}$ with a power of $\approx 50 \text{ mW}$ was used as the excitation source. The Rayleigh line was removed from the collected Raman signal by using a holographic notch filter located in the collection path. Figure S11 in the Supporting Information shows the in situ cell used for the Raman study. The airtight cell was made of polypropylene. Glass carbon (GC) substrates modified with different cathode materials (CNTs-NH₂@hemin, CNTs-OH@hemin, and CNTs-COOH@hemin electrodes) were placed into the cell from the bottom of the cell and used as working electrodes. A Pt wire was employed as the counter electrode. The electrolyte was 0.5 M Li₂S₈ solution prepared by adding sulfur and Li₂S at a molar ratio of 7:1 to an appropriate amount of anhydrous DMSO. The cell was assembled in an argon-filled glove box. An incident laser was introduced into the cell by passing through a flat Pyrex glass and focused onto the working electrode using a 50 \times objective lens. The distance between the electrode surface and the optically flat Pyrex glass was minimized (typically to 1 mm) to avoid scattering from the electrolyte. Electrochemical charge and discharge were performed using an electrochemical workstation (CHI760E, CH Instruments). All the Raman spectra in this study were recorded at various potentials during charge and discharge with a 10 s exposure time using a spectrometer equipped with a charge-coupled device (CCD) camera. All the spectra were calibrated to the 520 cm⁻¹ silicon line. Baseline corrections of the Raman spectra were performed using WiRE 4.0 software provided by Renishaw. All the experiments were performed at room temperature ($\approx 25 \text{ }^\circ\text{C}$).

In Situ FT-IRAS Measurements: In situ FT-IRAS measurements were performed on a Fourier-transform infrared spectrometer (iS50, Thermo Fisher) equipped with a liquid-nitrogen-cooled wide-band mercury-cadmium-telluride (MCT) detector. The spectroelectrochemical cell in this study is shown in Figure S12 in the Supporting Information. CNTs-COOH@hemin-coated carbon paper (CP) and Li foil were employed as the cathode and anode, respectively. A porous Celgard 2400 membrane was inserted between the cathode and anode as a separator. The cathode and Li anode were connected to the potentiostat using a Ti wire and a stainless-steel screw piton to achieve electrical contact, respectively. The bottom of the cell was sealed with a triangular diamond optical window and an o-ring to keep the electrolyte in the cell. Before the experiments, the polyetheretherketone (PEEK) cell and the optical window were cleaned in absolute ethanol using ultrasonication, followed by drying with nitrogen gas. To avoid strong IR absorption by the organic electrolyte, the cathode was pressed firmly against the diamond window using a screw mechanism to form a thin electrolyte layer ($\approx 1\text{--}2 \mu\text{m}$) between the cathode and window. At the experiment, the infrared light passed through the p-polarizer, and the obtained p-polarized light was used for in situ infrared research. The IR beam from the spectrometer was focused on the diamond/cathode interface at an incident angle of 45°. The reflected light was recollimated and focused on the MCT detector. During the measurements, the potential

was controlled using an electrochemical workstation (CHI760E, CH Instruments). The spectral resolution was set to 0.25 cm⁻¹, and four interferograms were coadded to each single-beam spectrum. The single-beam spectrum recorded at the initial 2.8 V was used as a reference. Finally, all the spectra were expressed in absorbance units defined as $A = -\log(R/R_0)$, where R and R_0 represent the reflectance intensity corresponding to the single-beam spectra recorded at sampling and reference potentials, respectively. Consequently, the upward and downward bands indicate an increase and decrease in the absorption intensities of the bands, respectively, at the sampling potential. For comparison, CNTs-NH₂@hemin and CNTs-OH@hemin electrodes were also used, and their performances were measured using the same method.

In Situ UV-Vis Spectroscopy Measurements: In situ UV-vis spectroscopic measurements were performed on an ultraviolet spectrophotometer (UV-1800, Malvern Panalytical). The spectroelectrochemical cell used in the present study is described in Figure S13 in the Supporting Information. The CNTs-COOH or CNTs-FG@hemin-coated GC electrode and platinum wire were employed as the cathode and anode, respectively. A 0.5 M Li₂S₈ solution was used as the electrolyte. During the measurements, the potential was controlled using an electrochemical workstation (CHI760E, CH Instruments). Here, the UV-vis absorbance was normalized by making the absorbance at 2.8 V as 1.

Computational Details: DFT calculations were performed using the all-electron code Fritz-Haber Institute ab initio molecular simulations package (FHI-aims).^[45] The Perdew-Burke-Ernzerhof (PBE) functional was used for structure relaxation,^[46] and the hybrid HSE06 functional was used for the electronic properties. The default “tight” basis sets and appropriate numerical settings were used in our work. To account for the weak noncovalent intermolecular interaction, these functionals were used in combination with the Tkatchenko-Scheffler correction.^[47] Ferritroporphyrin IX chloride (hemin, FePPCl) molecules anchored on the single-walled zigzag (16, 0) CNTs were proposed to simulate the active-site accessibility in the intermediate, LiPSs, and the vacuum layer between neighboring models was at least 12 Å to reduce the electrostatic interactions between them. The Brillouin zone was sampled using a 2 × 2 × 1 Monkhorst Pack k-point mesh during geometry optimization and a 3 × 3 × 1 k-point mesh for the electronic properties. For all of the complexes, spin polarization was used. The charge transfer between the LiPSs and hemin at the optimal configurations was performed using Mulliken charge analyses.^[48] The interaction between the hemin molecules and functionalized CNTs was evaluated using the binding energy, defined in Equation (1).

$$\Delta E_b = \Delta E_{\text{hemin+CNTs}} - \Delta E_{\text{CNTs}} - \Delta E_{\text{hemin}} \quad (1)$$

A more negative value of the binding energy indicated greater binding ability.

Supporting Information

Supporting Information is available from the Wiley Online Library or from the author.

Acknowledgements

X.D. and S.Y. contributed equally to this work. The work was supported in part by grants from National Natural Science Foundation of China (51972238, 21875166, 51920105004, 51572197), Natural Science Foundation of Zhejiang Province (LQ19B030006, LR18E020001), and General Research Foundation of Zhejiang Educational Committee (Y201839009), Science and Technology Project of Zhejiang Province (LGF18B050005). The authors are grateful to Chongqing Qindong Tech. Co. Ltd. for scientific computing assistance. The authors also thank Prof. Kohei Uosaki from National Institute for Materials Science (NIMS), Japan, for this helpful discussions and comments regarding this work.

Conflict of Interest

The authors declare no conflict of interest.

Keywords

biomimetic catalysis, hemin, lithium-sulfur batteries, polysulfides, structure-reactivity correlations

Received: April 15, 2020
Revised: May 15, 2020
Published online: July 9, 2020

- [1] H. J. Peng, J. Q. Huang, X. B. Cheng, Q. Zhang, *Adv. Energy Mater.* **2017**, *7*, 1700260.
- [2] A. Eftekhari, *ACS Sustainable Chem. Eng.* **2019**, *7*, 3684.
- [3] Y. X. Yin, S. Xin, Y. G. Guo, L. J. Wan, *Angew. Chem., Int. Ed.* **2013**, *52*, 13186.
- [4] J. He, Y. Chen, A. Manthiram, *Energy Environ. Sci.* **2018**, *11*, 2560.
- [5] Z. Xiao, Z. Yang, Z. Li, P. Li, R. Wang, *ACS Nano* **2019**, *13*, 3404.
- [6] Y. Fan, Z. Yang, W. Hua, D. Liu, T. Tao, M. M. Rahman, W. Lei, S. Huang, Y. Chen, *Adv. Energy Mater.* **2017**, *7*, 1602380.
- [7] Z. Li, J. T. Zhang, Y. M. Chen, J. Li, X. W. D. Lou, *Nat. Commun.* **2015**, *6*, 8850.
- [8] T. Zhou, W. Lv, J. Li, G. Zhou, Y. Zhao, S. Fan, B. Liu, B. Li, F. Kang, Q. H. Yang, *Energy Environ. Sci.* **2017**, *10*, 1694.
- [9] Z. Cheng, Z. Xiao, H. Pan, S. Wang, R. Wang, *Adv. Energy Mater.* **2018**, *8*, 1702337.
- [10] J. T. Yoo, S. J. Cho, G. Y. Jung, S. H. Kim, K. H. Choi, J. H. Kim, C. K. Lee, S. K. Kwak, S. Y. Lee, *Nano Lett.* **2016**, *16*, 3292.
- [11] H. Jiang, X. C. Liu, Y. Wu, Y. Shu, X. Gong, F. S. Ke, H. Deng, *Angew. Chem., Int. Ed.* **2018**, *57*, 3916.
- [12] Y. Song, W. Cai, L. Kong, J. Cai, Q. Zhang, J. Sun, *Adv. Energy Mater.* **2020**, *10*, 1901075.
- [13] S. Y. Lang, Y. Shi, Y. G. Guo, D. Wang, R. Wen, L. J. Wan, *Angew. Chem., Int. Ed.* **2016**, *55*, 15835.
- [14] S. Y. Lang, R. J. Xiao, L. Gu, Y. G. Guo, R. Wen, L. J. Wan, *J. Am. Chem. Soc.* **2018**, *140*, 8147.
- [15] Z. Xiao, Z. Yang, L. Zhang, H. Pan, R. Wang, *ACS Nano* **2017**, *11*, 8488.
- [16] I. Lieberman, P. Ove, *J. Biol. Chem.* **1958**, *233*, 634.
- [17] M. Shoji, K. Sato, H. Yukitake, Y. Kondo, Y. Narita, T. Kadowaki, M. Naito, K. Nakayama, *PLoS One* **2011**, *6*, e21372.
- [18] W. H. Ryu, F. S. Gittleson, J. M. Thomsen, J. Li, M. J. Schwab, G. W. Brudvig, A. D. Taylor, *Nat. Commun.* **2016**, *7*, 12925.
- [19] M. T. de Groot, M. Merckx, A. H. Wonder, M. T. M. Koper, *J. Am. Chem. Soc.* **2005**, *127*, 7579.
- [20] F. Valentini, L. Cristofanelli, M. Carbone, G. Palleschi, *Electrochim. Acta* **2012**, *63*, 37.
- [21] Y. Zhang, C. Xu, B. Li, *RSC Adv.* **2013**, *3*, 6044.
- [22] L. Gao, Y. Xiao, Y. Wang, X. Chen, B. Zhou, X. Yang, *Talanta* **2015**, *132*, 215.
- [23] C. Mateo, J. M. Palomo, G. Fernandez-Lorente, J. M. Guisan, R. Fernandez-Lafuente, *Enzyme Microb. Technol.* **2007**, *40*, 1451.
- [24] H. T. N. Le, H. K. Jeong, *Chem. Phys. Lett.* **2018**, *698*, 102.
- [25] Y. Zhang, M. Yang, N. G. Portney, D. Cui, G. Budak, E. Ozbay, M. Ozkan, C. S. Ozkan, *Biomed. Microdevices* **2008**, *10*, 321.
- [26] C. F. Guerra, J. W. Handgraaf, E. J. Baerends, F. M. Bickelhaupt, *J. Comput. Chem.* **2004**, *25*, 189.
- [27] M. Zhao, H. J. Peng, Z. W. Zhang, B. Q. Li, X. Chen, J. Xie, X. Chen, J. Y. Wei, Q. Zhang, J. Q. Huang, *Angew. Chem., Int. Ed.* **2019**, *58*, 3779.

- [28] L. Wang, Z. Yang, H. Nie, C. Gu, W. Hua, X. Xu, X. Chen, Y. Chen, S. Huang, *J. Mater. Chem. A* **2016**, *4*, 15343.
- [29] W. Hua, Z. Yang, H. Nie, Z. Li, J. Yang, Z. Guo, C. Ruan, X. Chen, S. Huang, *ACS Nano* **2017**, *11*, 2209.
- [30] G. Li, X. Wang, M. H. Seo, M. Li, L. Ma, Y. Yuan, T. Wu, A. Yu, S. Wang, J. Lu, Z. Chen, *Nat. Commun.* **2018**, *9*, 705.
- [31] J. Song, T. Xu, M. L. Gordin, P. Zhu, D. Lv, Y. B. Jiang, Y. Chen, Y. Duan, D. Wang, *Adv. Funct. Mater.* **2014**, *24*, 1243.
- [32] Z. Lin, T. Liu, X. Ai, C. Liang, *Nat. Commun.* **2018**, *9*, 5262.
- [33] J. Lei, F. McLarnon, R. Kostecki, *J. Phys. Chem. B* **2005**, *109*, 952.
- [34] H. J. Santner, C. Korepp, M. Winter, J. O. Besenhard, K. C. Moller, *Anal. Bioanal. Chem.* **2004**, *379*, 266.
- [35] E. L. Green, S. T. Taoka, R. Banerjee, T. M. Loehr, *Biochemistry* **2001**, *40*, 459.
- [36] J. P. M. Schelvis, V. Berka, G. T. Babcock, A. L. Tsai, *Biochemistry* **2002**, *41*, 5695.
- [37] L. Cheng, K. Yan, J. Zhang, *Electrochim. Acta* **2016**, *190*, 980.
- [38] Y. He, X. Wang, J. Sun, S. Jiao, H. Chen, F. Gao, L. Wang, *Anal. Chim. Acta* **2014**, *810*, 71.
- [39] J. Fan, M. Trenary, *Langmuir* **1994**, *10*, 3649.
- [40] B. S. Kim, S. M. Park, *J. Electrochem. Soc.* **1993**, *140*, 115.
- [41] N. Xu, T. Qian, X. Liu, J. Liu, Y. Chen, C. Yan, *Nano Lett.* **2017**, *17*, 538.
- [42] D. Chan, Z. Xiao, Z. Guo, Y. Lai, Y. Zhang, S. Zhou, X. Ding, H. Nie, Z. Yang, *Nanoscale* **2019**, *11*, 16968.
- [43] H. J. Peng, T. Z. Hou, Q. Zhang, J. Q. Huang, X. B. Cheng, M. Q. Guo, Z. Yuan, L. Y. He, F. Wei, *Adv. Mater. Interfaces* **2014**, *1*, 1400227.
- [44] Q. Zou, Y. C. Lu, *J. Phys. Chem. Lett.* **2016**, *7*, 1518.
- [45] V. Blum, R. Gehrke, F. Hanke, P. Havu, V. Havu, X. Ren, K. Reuter, M. Scheffler, *Comput. Phys. Commun.* **2009**, *180*, 2175.
- [46] G. Kresse, D. Joubert, *Phys. Rev. B* **1999**, *59*, 1758.
- [47] A. Tkatchenko, M. Scheffler, *Phys. Rev. Lett.* **2009**, *102*, 073005.
- [48] R. S. Mulliken, *J. Chem. Phys.* **1955**, *23*, 1841.